Micromechanical analyses of delamination, fracture and debonding in advanced composites

J.C.J. SCHELLEKENS and R. DE BORST
Delft University of Technology, Department of Civil Engineering /
TNO Building and Construction Research

Keywords: Micromechanics, interface elements, softening plasticity.

1. Introduction

In this contribution we shall present some current capabilities of DIANA for the analysis of advanced composite structure. We will present micromechanical analyses of matrix cracking in a ceramic composite and we will show some applications of interface elements for the modelling of fibre-matrix debonding and thermally induced delamination between the components of a PLCC-68 chip package.

The essence of interface elements is that they allow for a geometric discontinuity to occur in a structure. Depending on the constitutive model that is used to describe the inelastic response of the interface, the discontinuity may appear suddenly or can evolve gradually into a traction free internal boundary. An orthotropic softening plasticity model is presented which defines the relation between strength and stiffness degradation and crack opening in the interface elements. The quintessence of this modelling technique is that the surface under the softening curve is equal to the critical energy release rate G_c of the interface that fractures. This ensures on one hand a correct energy release during crack propagation, so that propagation is independent of the mesh refinement, and on the other hand it results in a proper description of the size effect (see Schellekens and De Borst 1992, Schellekens 1992).
In the next section the formulation of interface elements is presented. Attention is paid to the effect of the applied integration scheme on the element performance. In section 3 the formulation of the plasticity model is offered. Furthermore the algorithm for the elasto-plastic integration the derivation of the tangent stiffness relation are discussed. Finally the examples are presented in section 4.

2. Interface Elements

In this section a finite element formulation for line and plane interface elements is presented. Interface elements are a powerful tool in the modelling of geometrical discontinuities in different kinds of structures. In finite element analysis of civil engineering structures a large variety of applications for interface elements is present. Interface elements can be used to model soil-reinforcement interaction (Gens *et al.* 1988), to model the intermediate layer between rock and concrete e.g. in arch-dam analysis (Hohberg and Bachman 1989), or in the

analysis of rock-joints (Goodman *et al.* 1968, Gens *et al.* 1989). Applications in concrete mechanics cover the modelling of discrete cracking (Rots 1988), aggregate interlock (Feenstra *et al.* 1991) and bond between concrete and reinforcement (Keuser *et al.* 1983, Mehlhorn *et al.* 1985, Schäfer 1975). In rubber parts interface elements can be of importance when desintegration of rubber and texture is concerned e.g. in conveyor belts. Furthermore interface elements are suited to model delamination in layered composite structures (Schellekens and De Borst 1992, Schellekens 1992) or frictional contact in forming processes (Rodic and Owen 1989).

Interface elements can be divided into two elementary classes. A first class contains the continuous interface elements (line, plane and shell interfaces) which have been discussed in the literature by e.g. Goodman *et al.* (1968), Schäfer (1975), Mehlhorn *et al.* (1985) and Beer (1985), whereas the second class of elements contains the nodal or point interface elements (Ngo and Scordelis 1967), which, to a certain extent, are identical to spring elements. In this chapter we shall only consider the numerically and lumped integrated continuous interface elements. For a description of nodal or point interface elements the reader is referred to Ngo and Scordelis (1967) or Schellekens (1990).

2.1 Finite Element Formulation

As mentioned in the introduction the element stiffness matrix of line and plane interface elements can either be assembled by numerical or by lumped integration. The difference stems from the fact that in numerically integrated interfaces the traction-relative displacement relations are evaluated along an interpolated displacement field in the integration points, whereas the lumped interfaces evaluate the relation at the individual node-sets. In the following sections the formulation of numerically and lumped integrated elements is presented.

2.1.1 Numerically Integrated Interface Elements

Consider an nno-noded line or plane interface as in Figure 1. In a general 3D configuration each node has three translational degrees-of-freedom, which leads to an element nodal displacement vector $\mathbf{a}$

$$\mathbf{a} = \left(a_n^{\,1}, a_n^{\,2}, .., a_n^{\,nno}, a_s^{\,1}, a_s^{\,2}, .., a_s^{\,nno}, a_t^{\,1}, a_t^{\,2}, .., a_t^{\,nno} \right)^T , \tag{1}$$

where n denotes the direction normal to the interface surface and s and t denote the directions tangential to the interface surface as can be seen in Figure 1. The continuous displacement field is denoted as

$$\mathbf{u} = \left(u_n^{\,u}, u_n^{\,l}, u_s^{\,u}, u_s^{\,l}, u_t^{\,u}, u_t^{\,l} \right)^T \tag{2}$$

where the superscripts u and l indicate the upper and lower side or plane of the interface respectively. With aid of the interpolation polynomials $\mathbf{n} = (N_1, N_2, .., N_{nno/2})$ the relation between the continuous displacement field and the nodal displacement vector is derived as

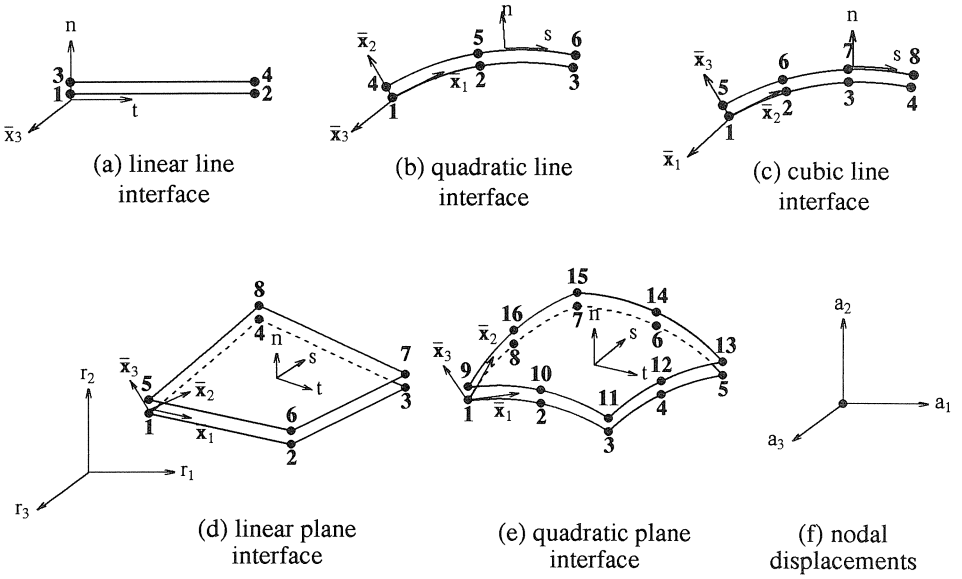

(a) linear line interface

(b) quadratic line interface

(c) cubic line interface

(d) linear plane interface

(e) quadratic plane interface

(f) nodal displacements

Figure 1 Line and plane interface elements

$$\mathbf{u} = \mathbf{H}\mathbf{a} \tag{3}$$

in which **H** contains the interpolation polynomials according to

$$\mathbf{H} = \begin{bmatrix} \mathbf{n} & 0 & 0 & 0 & 0 & 0 \\ 0 & \mathbf{n} & 0 & 0 & 0 & 0 \\ 0 & 0 & \mathbf{n} & 0 & 0 & 0 \\ 0 & 0 & 0 & \mathbf{n} & 0 & 0 \\ 0 & 0 & 0 & 0 & \mathbf{n} & 0 \\ 0 & 0 & 0 & 0 & 0 & \mathbf{n} \end{bmatrix}. \tag{4}$$

To relate the continuous displacement field to the relative displacements an operator matrix **L** is introduced

$$\mathbf{L} = \begin{bmatrix} -1 & +1 & 0 & 0 & 0 & 0 \\ 0 & 0 & -1 & +1 & 0 & 0 \\ 0 & 0 & 0 & 0 & -1 & +1 \end{bmatrix}. \tag{5}$$

When the relative displacement vector **v** is defined as $\mathbf{v} = (v_n, v_s, v_t)^T$ we obtain

$$\mathbf{v} = \mathbf{L}\mathbf{u}\,. \tag{6}$$

The relation between nodal displacements and relative displacements for continuous elements

is now derived from eqs. (3) and (6) as

$$\mathbf{v} = \mathbf{LHa} \quad \rightarrow \quad \mathbf{v} = \mathbf{Ba} \tag{7}$$

where the relative displacement-nodal displacement matrix $\mathbf{B}$ reads

$$\mathbf{B} = \begin{bmatrix} -\mathbf{n} & \mathbf{n} & 0 & 0 & 0 & 0 \\ 0 & 0 & -\mathbf{n} & \mathbf{n} & 0 & 0 \\ 0 & 0 & 0 & 0 & -\mathbf{n} & \mathbf{n} \end{bmatrix}. \tag{8}$$

If we consider an element in which the local coordinate systems in the integration points coincide with the global coordinate system, no transformations are necessary. For an arbitrary oriented interface element the matrix $\mathbf{B}$ has to be transformed to the local tangential coordinate system of the integration point or node-set. If the matrix $\mathbf{R}$ contains the local coordinate axes in the integration point, the transformation of the matrix $\mathbf{B}_g$ from the global coordinate system to the local axes ($\mathbf{B}_l$) in the integration point is given by $\mathbf{B}_l = \mathbf{B}_g\mathbf{R}^T$.

When the matrix $\mathbf{D}_I$ is used to denote the relation that describes the constitutive behaviour of the interface element

$$\mathbf{D}_I = \begin{bmatrix} d_n & 0 & 0 \\ 0 & d_s & 0 \\ 0 & 0 & d_t \end{bmatrix} \tag{9}$$

the traction-relative displacement relation becomes

$$\mathbf{t} = \mathbf{D}_I\mathbf{v} \tag{10}$$

in which $\mathbf{t} = (t_n, t_s, t_t)^T$ represents the traction vector.

In interface elements tractions and relative displacements are evaluated between the upper and the lower interface sides or planes. The components of the traction and relative displacement vector are determined by the orientations of the element sides or planes, and are thus fixed. The virtual work equation for an interface element can be written as

$$\delta W = \int_{S_0} \delta \mathbf{v}_j^T \mathbf{t}_j \, dS_0 \tag{11}$$

with S_0 the surface of the interface element. In a nonlinear analysis the traction vector at the end of an iteration j can be expressed as

$$\mathbf{t}_j = \mathbf{t}_{j-1} + \mathbf{D}_I \mathbf{dv}_j \tag{12}$$

where $\mathbf{dv}_j$ denotes the iterative change in the relative displacement vector. It can be demonstrated that variation of the relative displacement vector results in $\delta\mathbf{v}_j = \delta(\mathbf{dv}_j)$. Introducing eq. (12) in the virtual work expression and invoking (7) yields

$$\delta(\mathbf{da}_j)^T \int_{S_0} \mathbf{B}^T\mathbf{D}_I\mathbf{B} \, dS_0 \mathbf{da}_j = -\delta(\mathbf{da}_j)^T \int_{S_0} \mathbf{B}^T\mathbf{t}_{j-1} \, dS_0 \, . \tag{13}$$

The element stiffness matrix $\mathbf{K}$ and the internal force vector $\mathbf{f}_{j-1}$ can subsequently be defined as

$$\mathbf{K} = \int_{S_0} \mathbf{B}^T \mathbf{D}_I \mathbf{B}\, dS_0 \qquad \text{and} \qquad \mathbf{f}_{j-1} = -\int_{S_0} \mathbf{B}^T \mathbf{t}_{j-1}\, dS_0 \,. \tag{14}$$

For numerically integrated interface elements the integrals in eq. (14) are replaced by an integration over the iso-parametric coordinates ξ and η. For the element stiffness matrix of a plane interface element this gives

$$\mathbf{K} = \int_{\xi=-1}^{\xi=+1} \int_{\eta=-1}^{\eta=+1} \mathbf{B}^T \mathbf{D}_I \mathbf{B}\, \det\mathbf{J}\, d\xi\, d\eta \,. \tag{15}$$

In case of line interfaces the interpolation functions N_i are independent of η and eq. (15) reduces to

$$\mathbf{K} = b \int_{\xi=-1}^{\xi=+1} \mathbf{B}^T \mathbf{D}_I \mathbf{B} \left(\left(\frac{\partial x_1}{\partial \xi} \right)^2 + \left(\frac{\partial x_2}{\partial \xi} \right)^2 \right)^{1/2} d\xi \,. \tag{16}$$

where b is the width of the interface. If, for example, we use a 2×2 Gauß integration scheme for the assembly of the element stiffness matrix of a linear eight-noded plane interface with surface S, the result is

$$\mathbf{K} = \frac{1}{36} S \begin{bmatrix} \mathbf{K}_n & 0 & 0 \\ 0 & \mathbf{K}_s & 0 \\ 0 & 0 & \mathbf{K}_t \end{bmatrix} \tag{17}$$

where each 8×8 sub-matrix has the form

$$\mathbf{K}_i = \begin{bmatrix} 4d_i & 2d_i & d_i & 2d_i & -4d_i & -2d_i & -d_i & -2d_i \\ 2d_i & 4d_i & 2d_i & d_i & -2d_i & -4d_i & -2d_i & -d_i \\ d_i & 2d_i & 4d_i & 2d_i & -d_i & -2d_i & -4d_i & -2d_i \\ 2d_i & d_i & 2d_i & 4d_i & -2d_i & -d_i & -2d_i & -4d_i \\ -4d_i & -2d_i & -d_i & -2d_i & 4d_i & 2d_i & d_i & 2d_i \\ -2d_i & -4d_i & -2d_i & -d_i & 2d_i & 4d_i & 2d_i & d_i \\ -d_i & -2d_i & -4d_i & -2d_i & d_i & 2d_i & 4d_i & 2d_i \\ -2d_i & -d_i & -2d_i & -4d_i & 2d_i & d_i & 2d_i & 4d_i \end{bmatrix} \tag{18}$$

for i = n,s, and t. We notice that a full coupling between the nodal displacements of the node-sets is present in each specific direction.

2.1.2 *Lumped Integrated Interface Elements*

The major difference between lumped and numerically integrated interface elements is the use of relative displacements at the isolated node-sets instead of an interpolated relative displacement field in integration points. For the relative displacement vector $\mathbf{v}$ we now have

$$\mathbf{v} = \mathbf{B}_{is}\mathbf{a}, \tag{19}$$

with $\mathbf{B}_{is}$ the relative displacement-nodal displacement matrix for a node-set is. For a lumped interface element elaboration of the integral in eq. (15) results in a summation over the element node sets. Hence,

$$\mathbf{K} = \sum_{is=1}^{ns} \mathbf{B}_{is}{}^{T}\mathbf{D}_{I,is}\mathbf{B}_{is}S_{is} \tag{20}$$

where ns denotes the number of node sets and S_{is} is the surface contribution of node set is. Since the traction-relative displacement relation is evaluated in the individual node sets instead of in the integration points, the matrix $\mathbf{B}_{is}$ is obtained as

$$\mathbf{B}_{is} = \begin{bmatrix} -1 & +1 & 0 & 0 & 0 & 0 \\ 0 & 0 & -1 & +1 & 0 & 0 \\ 0 & 0 & 0 & 0 & -1 & +1 \end{bmatrix}. \tag{21}$$

With the sequence of element degrees of freedom as in eq. (1) this results in the following nodal displacement-relative displacement matrix $\mathbf{B}_1$ for the first node-set of a linear plane interface element:

$$\mathbf{B}_1 = \begin{bmatrix} -1 & 0 & 0 & 0 & 1 & 0 & 0 & 0 & 0 & 0 & 0 & 0 & 0 & 0 & 0 & 0 & 0 & 0 & 0 & 0 & 0 & 0 \\ 0 & 0 & 0 & 0 & 0 & 0 & 0 & 0 & -1 & 0 & 0 & 0 & 1 & 0 & 0 & 0 & 0 & 0 & 0 & 0 & 0 & 0 \\ 0 & 0 & 0 & 0 & 0 & 0 & 0 & 0 & 0 & 0 & 0 & 0 & 0 & 0 & 0 & 0 & -1 & 0 & 0 & 0 & 1 & 0 & 0 & 0 \end{bmatrix}. \tag{22}$$

The surface contributions S_{is} of the node-sets are determined from:

$$dS_{ip} = \det\mathbf{J}\, d\xi\, d\eta \tag{23}$$

and

$$S_{is} = \sum_{ip=1}^{nip} N_{is,ip}\, dS_{ip} \tag{24}$$

where $N_{is,ip}$ is the value of the interpolation polynomial of node-set is at integration point ip. As an example the stiffness matrix is given for an eight-noded linear plane interface with surface S:

$$\mathbf{K} = \frac{1}{4}S \begin{bmatrix} \mathbf{K}_n & 0 & 0 \\ 0 & \mathbf{K}_s & 0 \\ 0 & 0 & \mathbf{K}_t \end{bmatrix} \tag{25}$$

in which the eight by eight sub-matrix $\mathbf{K}_i$ has the form

$$\mathbf{K}_i = \begin{bmatrix} d_i & 0 & 0 & 0 & -d_i & 0 & 0 & 0 \\ 0 & d_i & 0 & 0 & 0 & -d_i & 0 & 0 \\ 0 & 0 & d_i & 0 & 0 & 0 & -d_i & 0 \\ 0 & 0 & 0 & d_i & 0 & 0 & 0 & -d_i \\ -d_i & 0 & 0 & 0 & d_i & 0 & 0 & 0 \\ 0 & -d_i & 0 & 0 & 0 & d_i & 0 & 0 \\ 0 & 0 & -d_i & 0 & 0 & 0 & d_i & 0 \\ 0 & 0 & 0 & -d_i & 0 & 0 & 0 & d_i \end{bmatrix} \tag{26}$$

where i can be n,s, and t. It is noted that in contrast to eq. (18) for lumped integration no coupling of degrees-of-freedom exists between the individual node sets.

2.1.3 Numerical Integration

In finite element analysis the surface or line integral to determine the element stiffness matrix is replaced by a weighted sum as

$$\mathbf{K} = \sum_{ip=1}^{nip} \alpha_{ip} A \, \mathbf{B}_{ip}{}^{T} \mathbf{D}_{ip} \mathbf{B}_{ip} \tag{27}$$

where the values of $\mathbf{B}_{ip}$ and the weight factor α_{ip} are dependent of the applied integration scheme and A is the surface of the element. For numerical integration of continuum elements the accurate Gauß scheme is commonly used, whereas thickness integration of shells is usually performed using a Simpson integration rule. However, in Gens *et al.* (1988), Rots (1988), Hohberg and Bachman (1989), Hohberg (1990), Schellekens (1990) and Qiu *et al.* (1992) it was found that under certain conditions the application of Gaußian integration to interface elements leads to oscillatory traction profiles owing to spurious kinematic element performance. In Schellekens and De Borst (1992), Schellekens (1992) a comprehensive study is presented on the influences of the applied numerical integration scheme on the element performance. There the conditions for spurious element performance are defined and an explanation for the undesired behaviour is offered. As a conclusion of the element study Table 1 can be constructed which connects the type of interface element to the optimal numerical integration rule(s). It is noted that the plus and minus sign refer to good and poor element performance.

Table 1 Effect of numerical integration scheme on the element performance

Integration Scheme	Element Type				
	Lin. Line	Quad. Line	Cub. Line	Lin. Plane	Quad. Plane
Gauß	-	-	-	-	-
Newton-Cotes	+	+	+	+	+
Lobatto	+	+	+-	+	+
Lumped	+	+	+	+	-

The fact that lumped integration fails to produce satisfactory results in case of a quadratic plane interface element is caused by the negative surface contributions of the corner nodes of quadratic elements which introduce negative diagonal terms in the element stiffness matrix. This leads to an ill-conditioned system of equations which is solved inaccurately with an LDU-decomposition without pivoting as has been done here.

Finally it is noted that the application of *linear* distorted plane interface elements produces inaccurate results when a Newton-Cotes or a Lobatto integration scheme is used to assemble the element stiffness matrix. This is caused by an improper calculation of the surface contributions (detJ) for the integration points. Elements that are integrated by a Gaußian integration scheme or a nodal lumping scheme do not suffer from this deficiency.

3. An Orthotropic Softening Plasticity Model for Interface Elements

For the modelling of mode-I interface fracture the discrete crack model described in Rots (1988) is sufficient. However, when the fracture in the interface is not purely of a mode-I type, and energy is also released in mode-II and mode-III, this discrete crack model is no longer applicable. To describe mixed-mode failure a constitutive model is required in which all three components of the traction vector t are involved. An orthotropic hardening/softening plasticity model now is proposed for the modelling of mixed-mode fracture in composites. The yield condition for interface plasticity is given by

$$\Phi(t,\kappa) = C_{nn}t_n^2 + C_{ss}t_s^2 + C_{tt}t_t^2 + C_n t_n - \bar{t}^2(\kappa) = 0 \tag{28}$$

with C_{ii} and C_n a set of material constants. t_n, t_s and t_t are the components of the traction vector. A cross section of the applied yield surface and the t_n,t_t plane is depicted in Figure 2. If $\bar{t}_n^c$ and $\bar{t}_n^t$ denote the compressive and tensile yield tractions in the direction normal to the

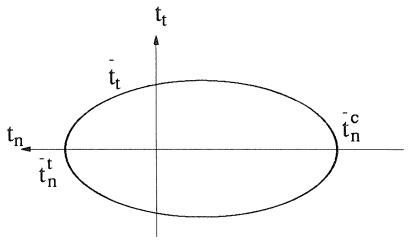

Figure 2 Yield surface for the orthotropic plasticity model

interface plane, $\bar{t}_s$ and $\bar{t}_t$ the shear yield tractions and $\bar{t}$ a normalised yield traction, substitution in condition (28) results in:

$$C_{nn} = \frac{\bar{t}^2}{\bar{t}_n^t \bar{t}_n^c} \quad C_{ss} = \frac{\bar{t}^2}{\bar{t}_s^2} \quad C_{tt} = \frac{\bar{t}^2}{\bar{t}_t^2} \quad C_n = \frac{\bar{t}^2}{\bar{t}_n^t} - \frac{\bar{t}^2}{\bar{t}_n^c} . \tag{29}$$

Recasting eq. (28) in matrix-vector notation yields

$$\Phi(\mathbf{t},\kappa) = \frac{1}{2}\mathbf{t}^T\mathbf{P}\mathbf{t} + \mathbf{t}^T\mathbf{p} - \bar{t}^2(\kappa) = 0 \tag{30}$$

in which $\mathbf{t}^T = (t_n, t_s, t_t)$, $\mathbf{P} = \text{diag}\,(2C_{nn}, 2C_{ss}, 2C_{tt})$ and $\mathbf{p}^T = (C_n, 0, 0)$.

As soon as this condition is satisfied, the total relative displacement rate $\dot{\mathbf{v}}$ is decomposed into an "elastic" part, $\dot{\mathbf{v}}^{el}$, and a "plastic" part, $\dot{\mathbf{v}}^{pl}$, as follows:

$$\dot{\mathbf{v}} = \dot{\mathbf{v}}^{el} + \dot{\mathbf{v}}^{pl} \tag{31}$$

The elastic relative displacement rate is related to the traction rate by

$$\dot{\mathbf{t}} = \mathbf{D}_I \dot{\mathbf{v}}^{el} , \tag{32}$$

and the assumption of an associated flow rule yields for the plastic relative displacement rate:

$$\dot{\mathbf{v}}^{pl} = \dot{\lambda}\frac{\partial\Phi}{\partial\mathbf{t}} . \tag{33}$$

For the present orthotropic yield criterion (30) this gives:

$$\dot{\mathbf{v}}^{pl} = \dot{\lambda}(\mathbf{P}\mathbf{t} + \mathbf{p}) . \tag{34}$$

Furthermore, we introduce the scalar κ as a measure for the amount of hardening or softening. In the case of a work hardening/softening hypothesis κ reads

$$\kappa = \int\dot{\kappa}dt \quad \text{with} \quad \dot{\kappa} = \mathbf{t}^T\dot{\mathbf{v}}^{pl} . \tag{35}$$

3.1 Integration of the Elasto-Plastic Relations

For finite increments of loading, eqs. (31) to (35) can be recast as:

$$\Delta \mathbf{v}_j = \Delta \mathbf{v}_j^{el} + \Delta \mathbf{v}_j^{pl} \tag{36}$$

$$\Delta \mathbf{v}_j^{el} = \mathbf{D}_I^{-1} \Delta \mathbf{t}_j \tag{37}$$

$$\Delta \mathbf{v}_j^{pl} = \Delta\lambda_j (\mathbf{P}\mathbf{t}_j + \mathbf{p}) \tag{38}$$

$$\Delta\kappa_j = \mathbf{t}_j^T \Delta \mathbf{v}_j^{pl} \tag{39}$$

A combination of these relations yields

$$\mathbf{D}_I^{-1} \Delta \mathbf{t}_j - \Delta \mathbf{v}_j + \Delta\lambda_j (\mathbf{P}\mathbf{t}_j + \mathbf{p}) = 0 \tag{40}$$

and finally

$$\mathbf{t}_j = (\mathbf{D}_I^{-1} + \Delta\lambda_j \mathbf{P})^{-1} (\mathbf{v}_{i-1}^{el} + \Delta \mathbf{v}_j - \Delta\lambda_j \mathbf{p}) \,. \tag{41}$$

Substitution of this expression for $\mathbf{t}_j$ in the yield condition (30) results in a nonlinear equation in $\Delta\lambda_j$: $\Phi(\Delta\lambda_j) = 0$, which can be solved by a local Newton-Raphson procedure:

$$\Delta\lambda_j^{k+1} = \Delta\lambda_j^k - \left. \frac{\Phi}{\dfrac{\partial \Phi(\Delta\lambda)}{\partial \Delta\lambda}} \right|_{\Delta\lambda_j^k} . \tag{42}$$

The derivative of $\Phi(\Delta\lambda_j)$ with respect to $\Delta\lambda_j$ in eq. (42) reads

$$\frac{\partial \Phi(\Delta\lambda_j)}{\partial \Delta\lambda_j} = \left(\frac{\partial \Phi}{\partial \mathbf{t}_j} \right)^T \frac{\partial \mathbf{t}_j}{\partial \Delta\lambda_j} + \frac{\partial \Phi}{\partial \kappa} \frac{\partial \kappa}{\partial \Delta\lambda_j} \tag{43}$$

and can be elaborated to give:

$$\frac{\partial \Phi(\Delta\lambda_j)}{\partial \Delta\lambda_j} = -(\mathbf{P}\mathbf{t}_j + \mathbf{p})^T (\mathbf{D}_I^{-1} + \Delta\lambda_j \mathbf{P})^{-1} \tag{44}$$

$$\left((\mathbf{D}_I^{-1} + \Delta\lambda_j \mathbf{P})^{-1} \mathbf{P} (\mathbf{v}_{i-1}^{el} + \Delta \mathbf{v}_j - \Delta\lambda_j \mathbf{p}) + \mathbf{p} \right) - h \,,$$

where

$$h = - \left. \frac{\partial \Phi}{\partial \kappa} \mathbf{t}^T \frac{\partial \Phi}{\partial \mathbf{t}} \right|_{\mathbf{t}_j} , \tag{45}$$

is the hardening modulus. The hardening/softening parameter κ is then updated according to

$$\Delta\kappa_j = \Delta\lambda_j \mathbf{t}_j^T (\mathbf{P}\mathbf{t}_j + \mathbf{p}) \tag{46}$$

3.2 The Consistent Tangent Operator for Orthotropic Plasticity

The derivation of the consistent tangent stiffness relation for orthotropic hardening/softening plasticity in interface elements is outlined below. Due to the hardening or softening type of response additional terms occur in the nonlinear equations which eventually result in a non-symmetric tangent stiffness relation.

The total relative displacement vector at the end of iteration j is given by

$$\mathbf{v}_j = \mathbf{v}_{i-1} + \Delta\mathbf{v}_j^{el} + \Delta\mathbf{v}_j^{pl} \tag{47}$$

where $\mathbf{v}_{i-1}$ is the relative displacement vector at the beginning of the loading step. With the relations for the incremental elastic and plastic relative displacements

$$\Delta\mathbf{v}_j^{el} = \mathbf{D}_I^{-1}\,(\mathbf{t}_j - \mathbf{t}_{i-1}) \tag{48}$$

and

$$\Delta\mathbf{v}_j^{pl} = \Delta\lambda_j \frac{\partial\Phi}{\partial\mathbf{t}_j} \tag{49}$$

the traction-relative displacement relation can be written as

$$\mathbf{v}_j = \mathbf{v}_{i-1} + \mathbf{D}^{-1}\,(\mathbf{t}_j - \mathbf{t}_{i-1}) + \Delta\lambda_j \frac{\partial\Phi}{\partial\mathbf{t}_j}\,. \tag{50}$$

The time derivative of eq. (50) reads

$$\dot{\mathbf{v}}_j = \mathbf{D}_I^{-1}\,\dot{\mathbf{t}}_j + \Delta\lambda_j \frac{\partial^2\Phi}{\partial\mathbf{t}_j^2}\dot{\mathbf{t}}_j + \dot{\lambda}\frac{\partial\Phi}{\partial\mathbf{t}_j}\,. \tag{51}$$

Introducing the relation for the plastic relative displacement rate in the consistency condition

$$\dot{\Phi} = \left(\frac{\partial\Phi}{\partial\mathbf{t}}\right)^T \dot{\mathbf{t}} + \frac{\partial\Phi}{\partial\kappa}\dot{\kappa} = 0 \tag{52}$$

leads to

$$\dot{\Phi} = \left(\frac{\partial\Phi}{\partial\mathbf{t}_j}\right)^T \dot{\mathbf{t}}_j + \Delta\lambda_j \frac{\partial\Phi}{\partial\kappa}\left(\frac{\partial\kappa}{\partial\mathbf{v}_j^{pl}}\right)\frac{\partial^2\Phi}{\partial\mathbf{t}_j^2}\dot{\mathbf{t}}_j + \dot{\lambda}_j \frac{\partial\Phi}{\partial\kappa}\left(\frac{\partial\kappa}{\partial\mathbf{v}_j^{pl}}\right)\frac{\partial\Phi}{\partial\mathbf{t}_j} = 0\,. \tag{53}$$

From this relation the time derivative of the plastic multiplier $\dot{\lambda}$ can be solved to be

$$\dot{\lambda}_j = \frac{1}{h}\left(\left(\frac{\partial\Phi}{\partial\mathbf{t}_j}\right)^T + \Delta\lambda_j \frac{\partial\Phi}{\partial\kappa}\left(\frac{\partial\kappa}{\partial\mathbf{v}_j^{pl}}\right)\frac{\partial^2\Phi}{\partial\mathbf{t}_j^2}\right)\dot{\mathbf{t}}_j \tag{54}$$

in which h is given by eq. (45). Substituting the above expression for $\dot{\lambda}$ in eq. (51) subsequently yields for the relative displacement rate $\dot{\mathbf{v}}_j$

$$\dot{v}_j = \left[D_I^{-1} + \Delta\lambda_j \frac{\partial^2 \Phi}{\partial t_j^2} + \frac{1}{h} \frac{\partial \Phi}{\partial t_j} \left(\frac{\partial \Phi}{\partial t_j} \right)^T + \frac{\Delta\lambda_j}{h} \frac{\partial \Phi}{\partial \kappa} \left(\frac{\partial \Phi}{\partial t_j} \right) \left(\frac{\partial \kappa}{\partial v_j^{pl}} \right) \frac{\partial^2 \Phi}{\partial t_j^2} \right] \dot{t}_j \,. \tag{55}$$

At this point a matrix $\mathbf{H}$ is introduced

$$H = D^{-1} + \Delta\lambda_j \frac{\partial^2 \Phi}{\partial t_j^2} + \frac{\Delta\lambda_j}{h} \frac{\partial \Phi}{\partial \kappa} \underline{\left(\frac{\partial \Phi}{\partial t_j} \right) \left(\frac{\partial \kappa}{\partial v_j^{pl}} \right)} \frac{\partial^2 \Phi}{\partial t_j^2} \tag{56}$$

The underlined part in eq. (56) introduces the non-symmetry in the matrix $\mathbf{H}$, which renders the tangential stiffness matrix to be non-symmetric (see eq. (58)). With eq. (56) eq. (55) can conveniently be rewritten as

$$\dot{v}_j = \left[H + \frac{1}{h} \frac{\partial \Phi}{\partial t_j} \left(\frac{\partial \Phi}{\partial t_j} \right)^T \right] \dot{t}_j \tag{57}$$

Use of the Sherman-Morrison-Woodbury formula then yields the consistent tangent stiffness relation

$$\dot{t}_j = \left[H^{-1} - \frac{H^{-1} \left(\frac{\partial \Phi}{\partial t_j} \right) \left(\frac{\partial \Phi}{\partial t_j} \right)^T H^{-1}}{h + \left(\frac{\partial \Phi}{\partial t_j} \right)^T H^{-1} \left(\frac{\partial \Phi}{\partial t_j} \right)} \right] \dot{v}_j \,. \tag{58}$$

3.3 Model Assumptions

Due to the fact that we intend to model both plasticity and cracking in the interface we can no longer regard the inelastic deformations as being purely plastic. We define the inelastic relative displacements as crack relative displacements ($\mathbf{v}^{cr}$) except for the mode-I inelastic relative displacements that are induced by a compressive loading. These are considered as plastic (see Figure 3). The degradation of the elastic properties of the interface is coupled with the inelastic relative displacement due to cracking ($\mathbf{v}^{cr}$). In this case the stiffness that determines the tractions in unloading or reloading is the so-called secant stiffness matrix denoted by $\mathbf{D}_I^s$. From the moment of crack-closure (defined by $v_n \leq v_n^{pl}$), that is in the compressive loading regime, the initial elastic stiffness governs the interface behaviour. It is assumed that due to the irreversible plastic relative displacements that may occur, the traction relative displacement diagram shifts horizontally over a distance v_n^{pl} (see Figure 3). Furthermore the assumption is made that the degradation of the equivalent yield traction $\bar{t}$ is not influenced by yielding in compression. Thus the amount of inelastic work that is used to determine $\bar{t}$ and C_n is defined

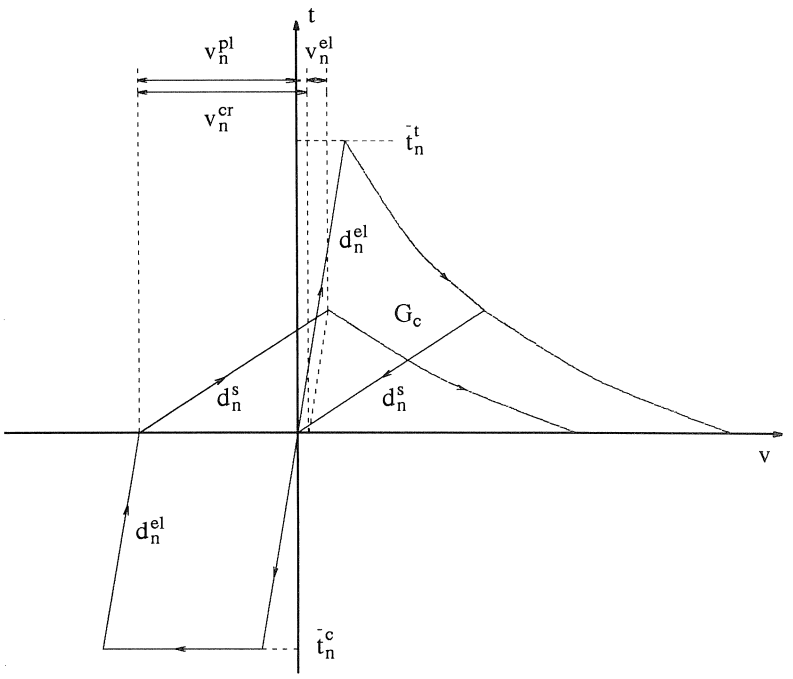

Figure 3 Traction relative displacement relation for the mode-I component

as $\dot{\kappa} = \mathbf{t}^T \dot{\mathbf{v}}^{cr}$. In the analyses that are presented in the next section a linear relation between κ and $\bar{t}$ has been assumed: $\bar{t} = \bar{t}_0(1-\kappa/G_c)$, where $\bar{t}_0$ denotes the initial transverse tensile strength of the interface and G_c denotes the fracture toughness of the material.

4. Applications

This section presents some applications of interface elements and the interface constitutive models in micro and macro-mechanical analyses of advanced composite materials. In the first and the second example interface elements are used in a micro-mechanical analysis of fibre-matrix debonding and the interaction of debonding with matrix fracture. A third example concerns the application of interface elements to a three-dimensional analysis of thermally induced delamination in a PLCC-68 chip package. Due to thermal cyclic loading delamination is induced between the chip and the surrounding epoxy. In the computations presented in this section a full Newton-Raphson method has been adopted, whereas a variation of 10^{-4} on the energy was taken as a convergence criterion. The analyses of sections 4.1 and 4.2 have been carried out under arc-length control.

4.1 Micromechanical Analyses of Composite Fracture

Since a poor bonding between fibres and matrix limits the possibilities of composites constituted of high performance fibres, at present a great deal of effort is put in understanding the interaction between fibres and matrix and improving the interface bonding. In the first example a micro-mechanical analysis of a metal-matrix composite is presented (see Jones *et al.* 1991). Starting from a micro-mechanics level where the stress-strain relation is determined for a representative volume element (RVE), the homogenised response for the macroscopic level, in which the effects of matrix nonlinearities and fibre-matrix debonding are included, can be derived. Furthermore micro-mechanical analyses can be used in order to quantify the effects of fibre volume fraction, interface characteristics, matrix properties and the presence of micro-cracks on the overall composite properties and behaviour.

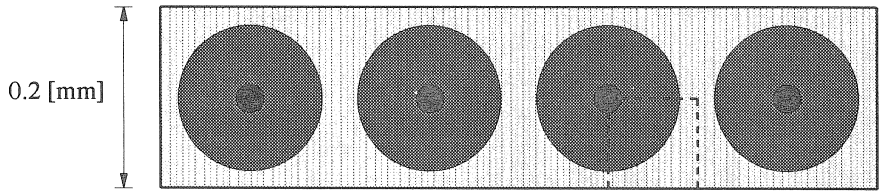

$E_m^{el} = 147.0$ GPa $\quad E_f = 413.7$ GPa

$\nu_m = 0.3 \quad \nu_f = 0.2$

$\bar{\sigma}_m = 96.5$ MPa

$E_m^{pl} = 14.7$ MPa

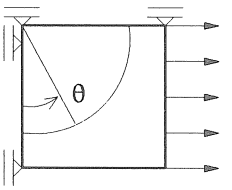

Figure 4 Geometry and properties of the composite ply

A single ply of a metal-matrix composite with Silicon Carbide fibres (50% fibre volume fraction) is loaded in transverse tension (Figure 4). Since in the composite ply we have a periodic arrangement of the fibres the choice of the RVE is evident. Due to symmetry only a quarter of the RVE was discretised using 204 and 860 quadratic plane strain triangles as is shown in Figure 5. In the vertical direction free contraction of the RVE is allowed whereas an equal displacement constraint was imposed on the nodes of the right boundary. Between the matrix and the fibre interface elements are introduced as to account for debonding failure.

The material properties that have been adopted in the analyses for the 304 stainless steel matrix and the SCS-6 SiC fibres are are taken from Jones *et al.* (1991). The nonlinear matrix behaviour has been modelled by a Von Mises plasticity model with isotropic linear hardening ($E^{pl} = 0.1\ E^{el}$). It is noted that the properties are specified at a temperature of 922K. For the interface elements a dummy stiffness equal to $d_n = d_s = 10^{+7}$ was supplied. The tensile,

compressive and shear strength for the orthotropic plasticity model were all chosen equal to 72.5 N/mm^2. A work softening hypothesis has been used with G_c = 50.0 N/m substituted for the fracture toughness of the interface.

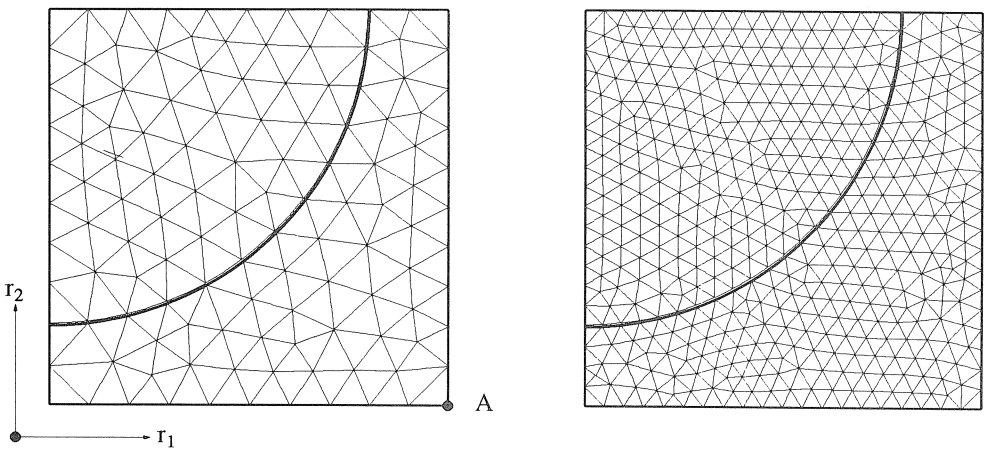

Figure 5 Finite element discretisation of a quarter of the RVE

In Figure 6 for different load levels the shear (dashed lines) and normal tractions (solid lines) are depicted along the interface as a function of the angle θ, for different load levels. For the load level of 2.5 [N] the curves represent the elastic tractions in the interface, whereas a load level of 2.47 [N] refers to an almost completely debonded stage. We clearly observe the redistribution of stresses due to failure of the fibre-matrix interface.

The load-displacement curves for both the coarse and the fine mesh are presented in Figure 7 which show a mesh-insensitive response.

A plot which shows the equivalent plastic strain contours in the deformed model is presented in Figure 8. The corresponding displacement of point A is equal to $5.6\,10^{-3}$ mm (F = 2.66 [N]), whereas the scale of deformation in this picture is 1.0.

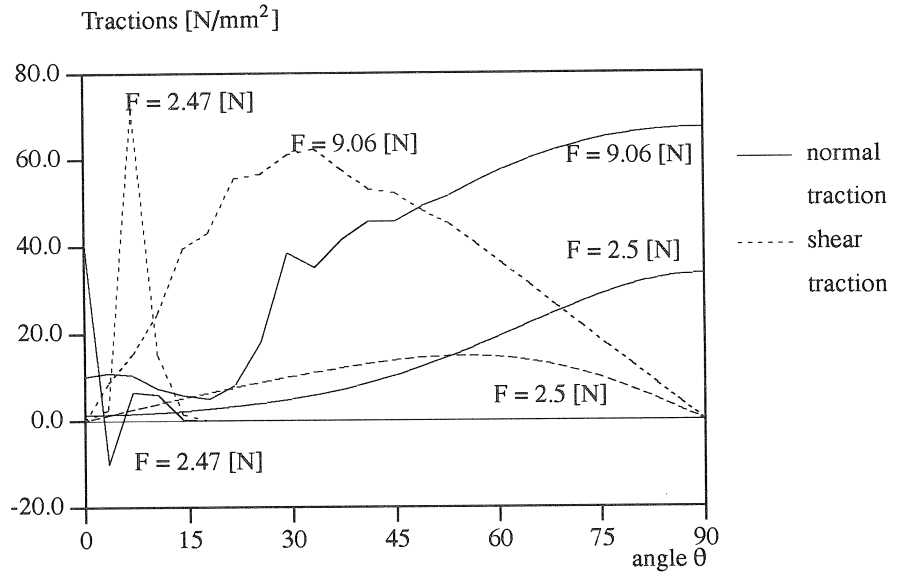

Figure 6 Normal and shear tractions along the fibre matrix interface (coarse mesh)

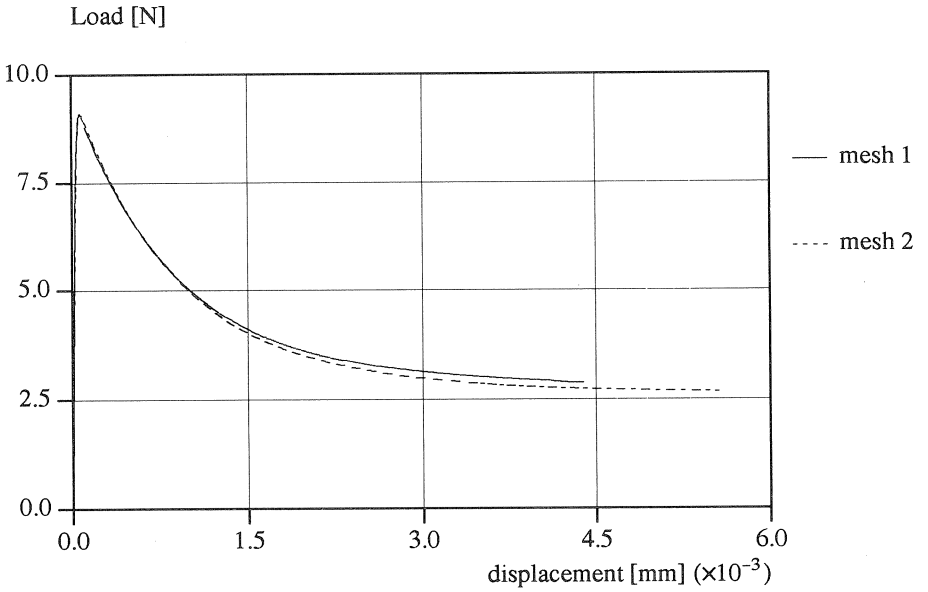

Figure 7 Load-displacement curves for point A

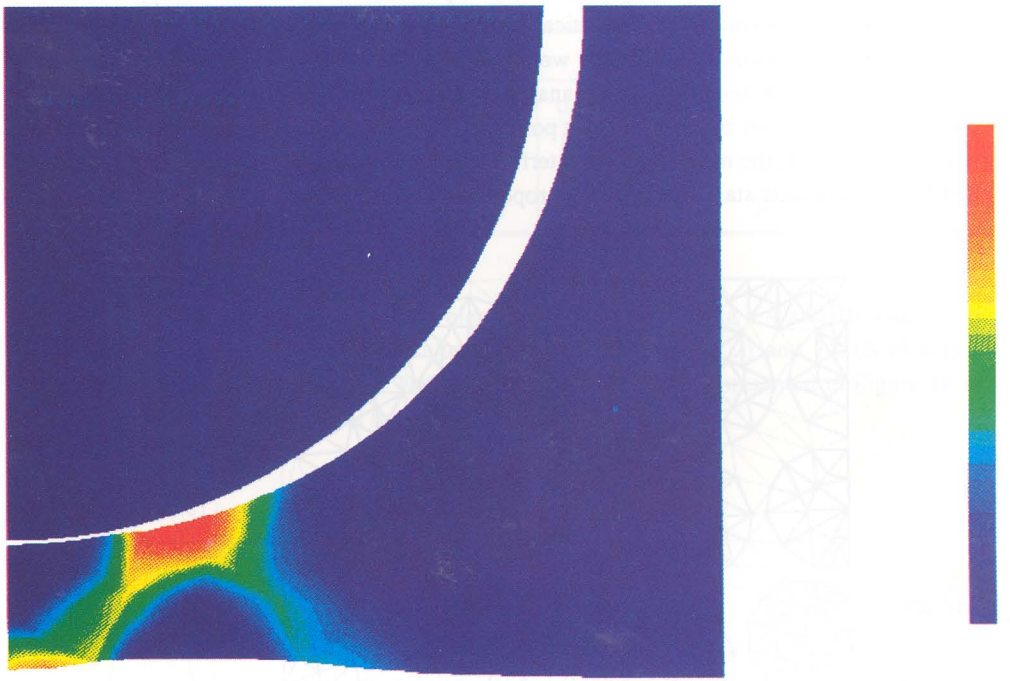

Figure 8 Equivalent plastic strains in the deformed geometry

4.2 Matrix Cracking

The second application concerns a micro-mechanical analysis of a ceramic composite where the attention is focused on matrix fracture. For cement-based composites similar analyses have been presented in Willam (1989) and Roelfstra (1989).

In this example the effects of mesh-refinement on the results are investigated and the limitations of the used constitutive models are discussed. In Figure 9 a finite element discretisation of a elementary volume is presented (Weihe 1992)[1]. The dimensions of the finite element model are 30×30 microns. The fibre diameter has a normal distribution with an average fibre diameter of 6.293 μm with a standard deviation of 0.212 μm. The finite element mesh consists

1 The mesh generator for the finite element discretisations presented in this section has been developed by Dipl.-Ing. S. Weihe of the Institute for Statics and Dynamics of Aerospace Structures of the University of Stuttgart, Germany. His cooperation in providing the finite element meshes is gratefully acknowledged.

of linear plane-stress triangles which are integrated by a single point rule. For the left boundary the translations in the horizontal direction are prevented, whereas for the upper and lower boundary the displacements in the vertical direction are suppressed. For the right side the displacements in the horizontal direction were forced to be equal. The structure is loaded by an edge load at the right boundary. In the analyses an arc-length control method was necessary to continue to calculation beyond the limit point. Method A was used for automatic load estimation. For the fibres, the matrix and the interface elements, which were inserted in the finite element model at a later stage, the material properties are listed in Table 2.

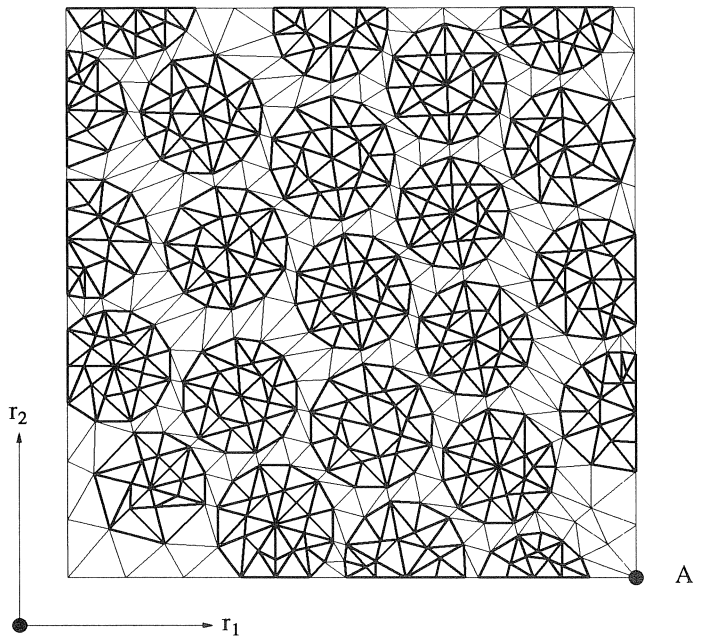

Figure 9 Finite element model

In a first series of analyses the effect of mesh refinement on the results is examined. Cracking of the matrix material was simulated using a Von Mises plasticity model. A work softening hypothesis has been adopted with a linear relation between κ and $\bar{\sigma}$:

$$\dot{\kappa} = \frac{1}{\bar{\sigma}} \sigma^T \dot{\varepsilon}^{pl} \quad \text{and} \quad \bar{\sigma} = \bar{\sigma}_0 \left(1 - \frac{\kappa}{\kappa_u} \right) \quad \text{where} \quad \kappa_u = \frac{2G_c}{\bar{\sigma}}$$

Table 2 Material properties

	Fibres	Matrix	Interface Elements	
E [N/mm^2]	140000	10000	d_n, d_s [N/mm^3]	100.0
ν	0.2	0.3	$\bar{t}_n^t, \bar{t}_n^c$ [N/mm^2]	100.0
$\bar{\sigma}$ [N/mm^2]	-	100.0	$\bar{t}_s$ [N/mm^2]	100.0
G_c [N/m]	-	10.0	G_c [N/m]	100.0

The original configuration (Mesh 1, 973 elements) of Figure 9 using a 4 and 16 times finer finite element discretisation which resulted in a total 3892 (Mesh 2) and 15568 elements (Mesh 3) for the respective models. The results of the analyses are presented in Figure 10 in terms of load-displacement curves for point A at the right boundary.

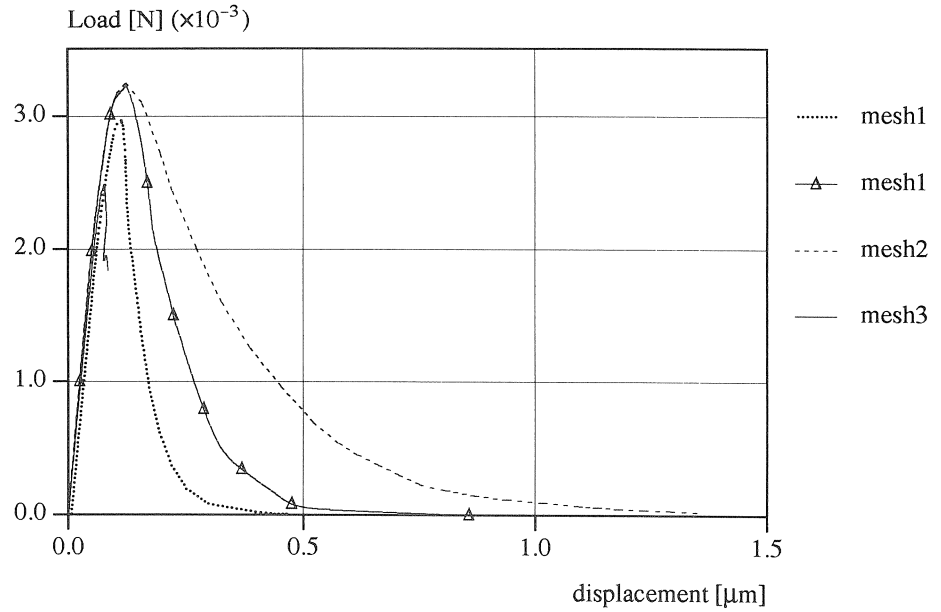

Figure 10 Load-displacement curves for point A.

Obviously the results are highly dependent on the discretisation. This is inherent in numerical simulations of structural failure where the failure is initiated by a softening material response and a classical continuum description is used (Bazant 1976, De Borst 1986). The structure behaves more brittle upon mesh-refinement and the amount of dissipated energy reduces to

zero. The underlying reason for the observed phenomenon of mesh-dependence is the fact that the system of governing differential equations becomes hyperbolic due to the incorporation of softening in the material model. The ensuing loss of well-posedness of the boundary value problem (Benallal *et al.* 1991) triggers the occurrence of spurious kinematic modes (De Borst and Rots, 1989).

For mesh 1 two load-displacement curves are presented. The dotted line corresponds to a solution with two localisation bands (Figure 11) whereas the solid line with the marker represents a solution with only one band (Figure 12) which was obtained for a lower value of the initial load parameter. Hence, the obtained solution is highly path dependent.

In Figures 11 to 14 the deformed geometries are presented at the end of the calculations when the imposed load has been reduced to zero (except for mesh 3 where it was not possible to continue the calculation to a zero residual load level). The deformations localise in a zone with a width that is equal to the element length. The fact that the location of the localisation band changes in Figures 12 to 14 is purely the result of the geometrical imperfections that are introduced in the mesh during mesh-refinement.

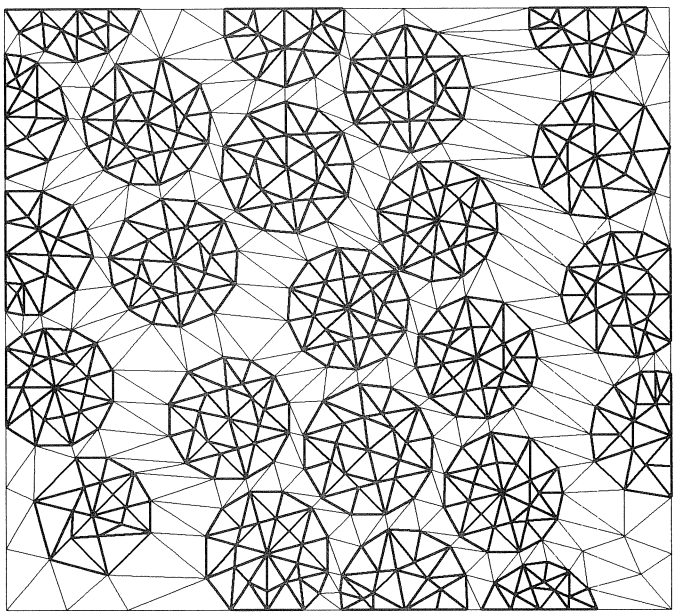

Figure 11 Deformed model Mesh 1

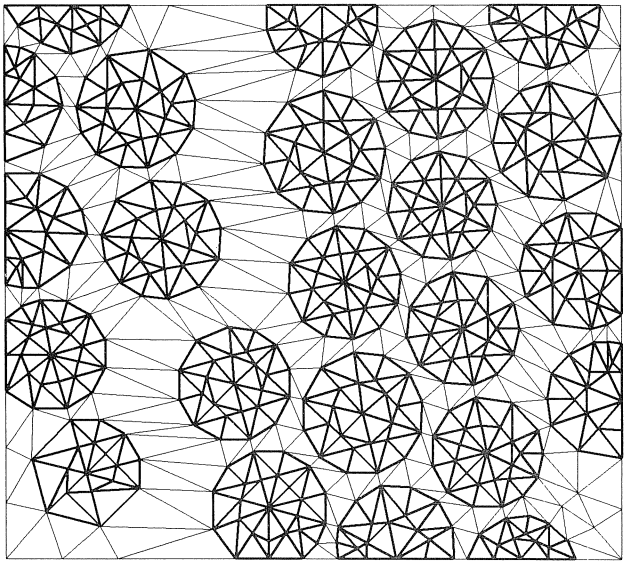

Figure 12 Deformed model Mesh 1

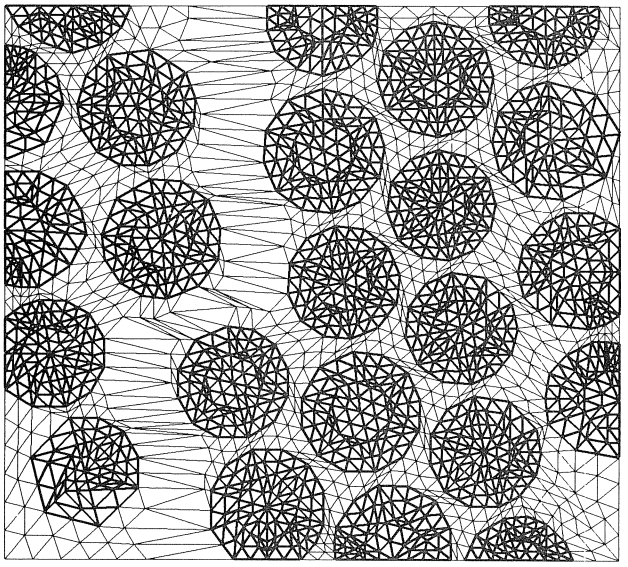

Figure 13 Deformed model Mesh 2

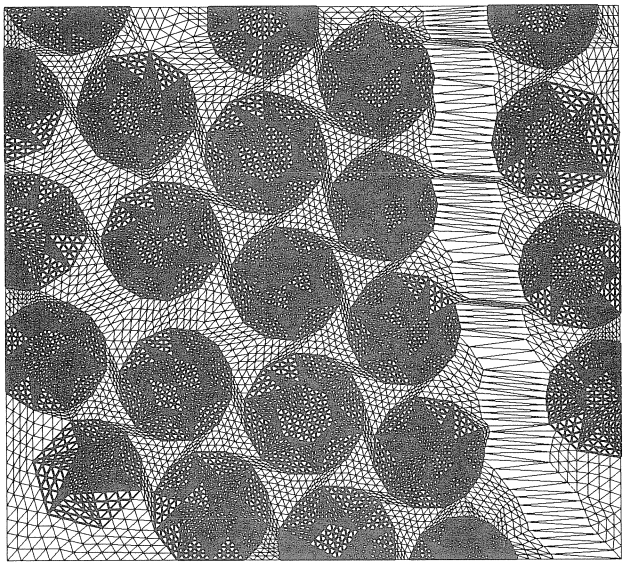

Figure 14 Deformed model Mesh 3

In the next series of analysis the constitutive model is slightly modified in the sense that now the square root of the element surface S is used to obtain an objective energy release upon mesh-refinement ($G_c = \sqrt{S} \int \sigma^T d\varepsilon^{pl}$) (Bazant and Oh 1983, Willam 1984). Although this numerical artefact does not preserve the ellipticity of the system of equations and still results in a localisation band of decreasing width when the finite element discretisation is further refined, it achieves a mesh objective response on a global structural level. The results of the analyses in which the crack band is included are presented in Figure 15 in terms of load-displacement curves. In these analyses the amount of dissipated energy is almost constant upon mesh-refinement. Figure 16 shows that in this case also for the coarse mesh a single localisation band is obtained, although at a different location than in Figure 10.

In order to preserve the well-posedness of the boundary value problem a higher order continuum description should be used (gradient plasticity, Mühlhaus and Aifantis 1991, De Borst and Mühlhaus 1992). However it is doubted that for this specific problem a gradient theory will offer a solution since it requires C^1 continuity of the plastic multiplier, which is an element degree-of-freedom. To date this has not yet been accomplished for triangular elements. The application of a non-local damage formulation (Pijaudier-Cabot and Bazant 1987) or micro-polar continuum formulation (Mühlhaus and Vardoulakis 1987, De Borst 1991) to solve the problem of spurious localisations is believed to be more promising. Since in this particular case the micro-rotations and couple-stresses of the elements, which introduce the necessary length scale in the constitutive model, will be actived by a considerable amount of shear deformation. However, the fact that also energy is dissipated in mode-I may disturb the regularising effect (Sluys 1992).

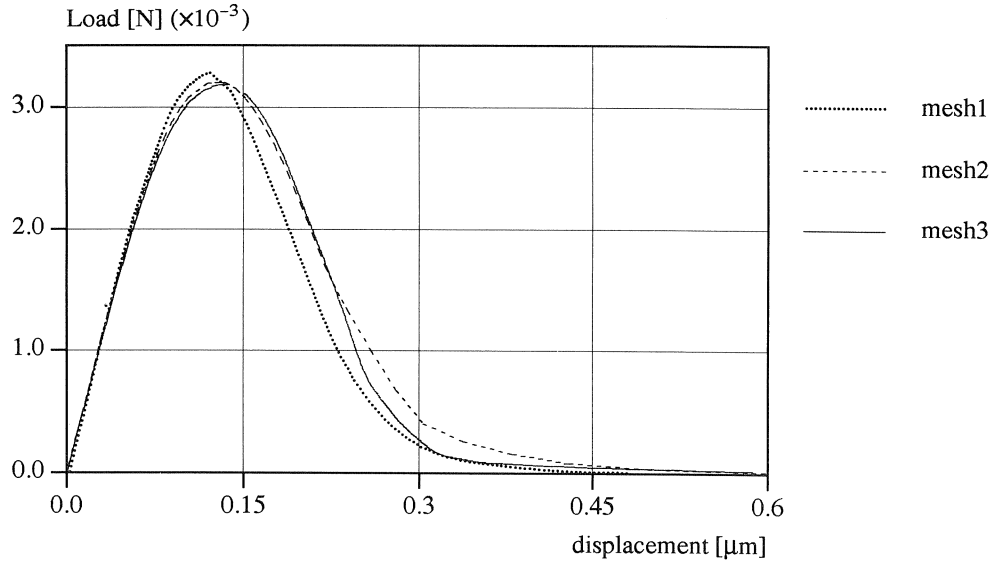

Figure 15 Load-displacement curves for point A

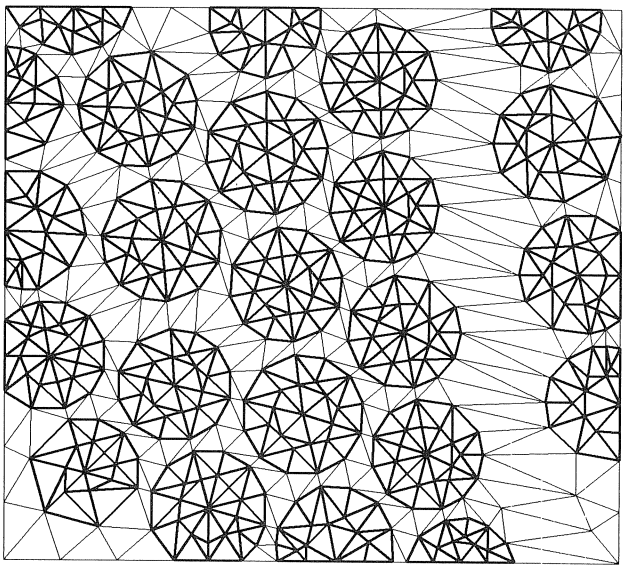

Figure 16 Deformed model Mesh 1, using a crack band

For mesh 2 the equivalent plastic strains at a zero residual load level are shown in Figure 17. It is observed that there is an accumulation of plastic strains in a band having a width of a single element. No continuous transition of the equivalent plastic strains exist on the element boundary, which is physically not realistic.

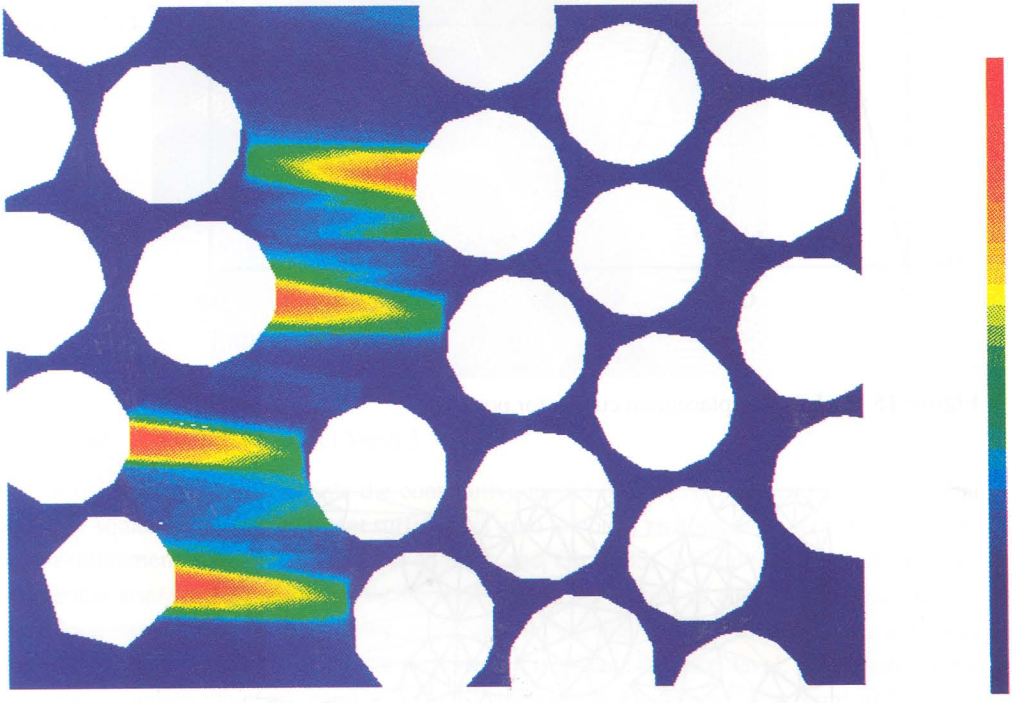

Figure 17 Equivalent plastic strains in the matrix. Scale of deformation equal to 20

Figure 18 shows the influence of the yield strength of the matrix on the composite behaviour. The value of $\bar{\sigma}$ was varied between 25.0 and 100 N/mm^2. One would expect that for a constant value of the fracture toughness G_c the steepness of the descending branch would increase and the maximum displacement would decrease. However, we observe that the curve for $\bar{\sigma}$ = 75.0 N/mm^2 does not follow this tendency. A plot of the deformed model showed that in this case not one but two localisation bands exist, which corresponds with the existence of 2 negative diagonal terms in the structural stiffness matrix. This explains the almost double amount of energy that is consumed before the load has reduced to zero. After decreasing the value of the initial load parameter a solution was obtained with only one localisation band, which corresponds to the lowest energy path. Which localisation band or bands are activated is not only dependent on the geometrical imperfections, but also on the combination of the

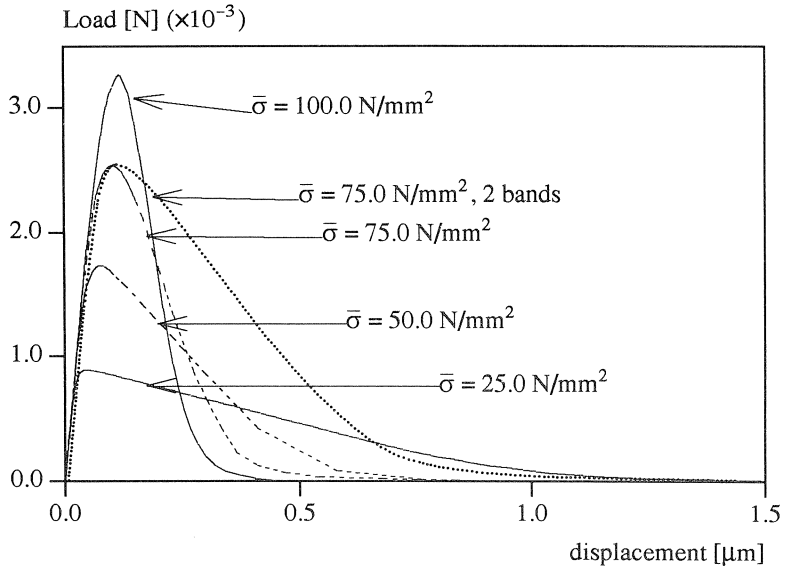

Figure 18 Load-displacement curves for point A as a function of $\bar{\sigma}$

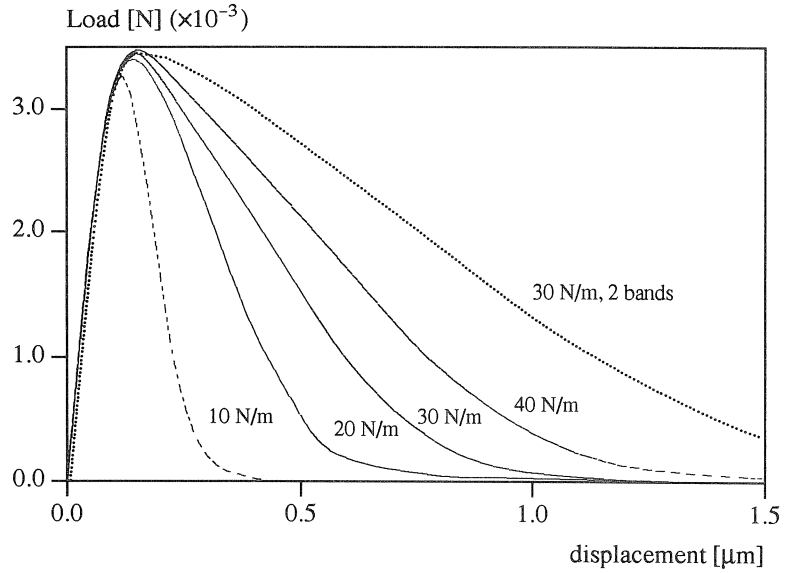

Figure 19 Load-displacement curves for point A as a function of G_c

model parameters and the value of the initial load parameter. Figure 18 furthermore shows that the dependency of the peak load on the yield value is almost linear. A similar result as described above was found for a variation of the fracture toughness of the matrix (see Figure 19). For G_c equal to 30.0 N/m solutions with one and two localisation bands were obtained depending on the value of the initial load parameter $\Delta\mu_0$. Again the lowest energy path was traced using a smaller value for $\Delta\mu_0$. The curves presented in Figure 19 reveal that the ultimate load is hardly effected by the value of the fracture toughness and that the deformation capacity of the reference volume increases linearly with the value of G_c.

4.3 Thermally Induced Delamination in a Chip-Package [1]

In this section a simulation of delamination failure in a PLCC-68 chip package in a temperature cycle test is presented. Usually these tests are performed to accelerate the occurrence of different failure mechanisms in the package. Once the dominating failure modes are known the package design is adjusted in order to eliminate them.

During the assembly of a chip package the silicon die or chip is glued onto a CuFe die-support paddle. Then the gold bonding bond wires are attached, which connect the aluminium pattern on the die surface with the lead frame. Finally the epoxy coating is applied through injection moulding (Van Gestel 1990).

In experiments it has been observed, that when these packages are imposed to high temperature cycles, high in-plane shear stresses occur at the chip surface, especially near the corners. This is a result of the mismatch in thermal expansion coefficients of the different components. Eventually these stresses will induce delamination cracks between the chip and epoxy coating which may result in bond-wire failure, pattern shift on the chip surface and cracks in the chip.

In the finite element model interface elements are inserted between the lead-frame and the epoxy as well as between die-support paddle, chip and epoxy (r_3 = 1.45 mm, r_3 = 1.85 mm and r_3 = 2.25 mm). Due to computer limitations a complete nonlinear analysis of the original finite element model which consisted of a total number of 9434 volume and interface elements was not feasible. Therefore a new model was prepared in which not all the members of the lead frame were incorporated. The parts of the finite element model are presented in Figures 20 to 22.

---

1 The work described in this section is the result of joint research of the author and ir. H.C.J.M. van Gestel of the Faculty of Electrical Engineering of the Delft University of Technology. The author wishes to thank ir. v. Gestel for the preparation of the finite element meshes presented in this section.

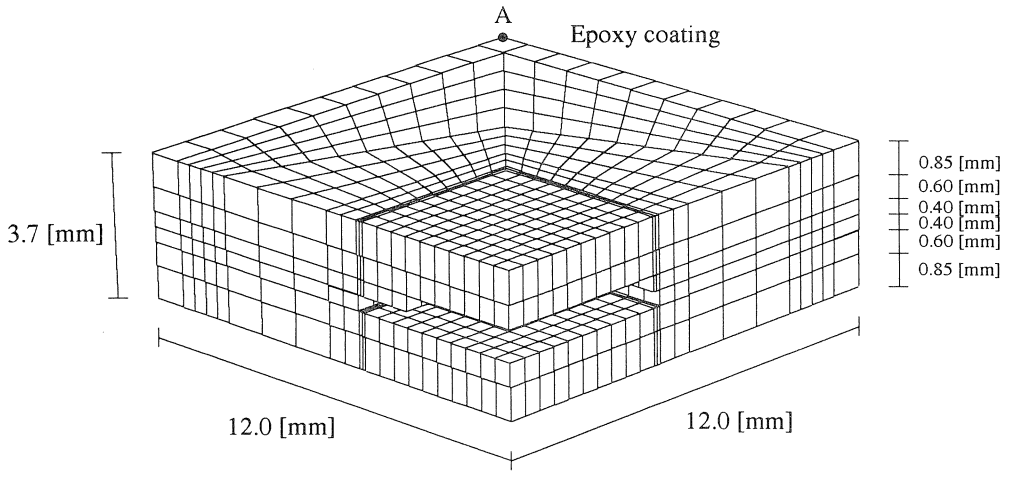

Figure 20 Finite element model of the PLCC-68 chip package.

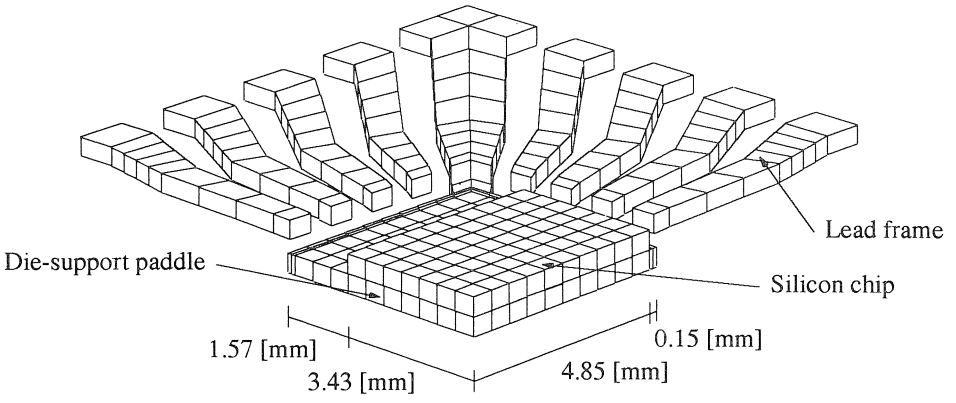

Figure 21 Lead frame, die-support paddle and chip

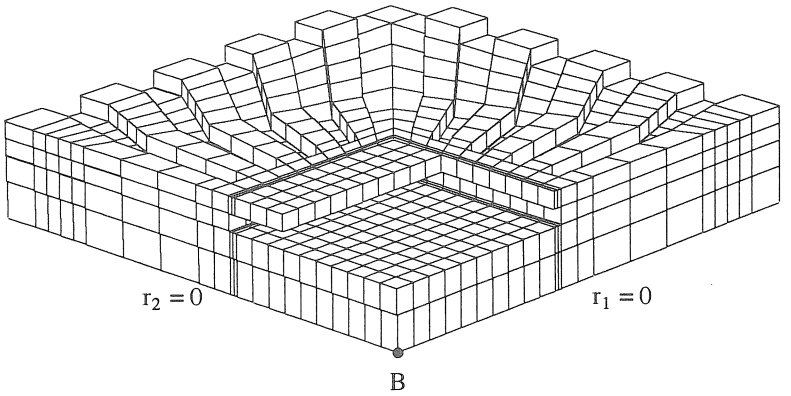

Figure 22 Finite element model of the lower half of the epoxy coating

2046 linear brick and 1023 linear plane interface elements have been used to model a quarter of the chip package. The only boundary condition that was imposed on the structure was the restrained displacement of point B in the vertical direction (Figure 22). The symmetry planes are given by $r_1 = 0$ and $r_2 = 0$ as indicted in Figure 22.

The material properties of the different materials are listed in Table 3. The physically non-linear behaviour of the interface elements is described by the orthotropic plasticity model and linear work softening response has been adopted. For the different interfaces the properties are presented in Table 4.

A minor modification to the plasticity model was made in order to incorporate the influence of fatigue on the interface strength. In the analysis it has been assumed that during each temperature cycle the value of κ increases with 10.0% of the fracture toughness of the interface. Although it is recognised that this is an arbitrary assumption, it is justified by the fact that the intention of the analysis is to be purely qualitative. In the analysis the PLCC package is imposed to 10 temperature cycles. The start temperature is 180.0 °C at which the chip is assumed to be stress free. Then the temperature cycles start with cooling down to -65.0 °C and then heating up to 165.0 °C. This amplitude in temperature of 230.0 °C is then maintained during the rest of the cycles.

Table 3 Material properties PLCC-68 package

	epoxy coating	lead-frame/die-paddle	chip
E [N/mm^2]	15000.0	119000.0	131000.0
ν	0.25	0.3	0.3
α [1/°C]	20.0 10^{-6}	17.0 10^{-6}	23.0 10^{-6}

Table 4 Material properties for interface elements

	Interface		
	epoxy/metal	die-paddle/chip (glue)	chip/epoxy
d_i [N/mm^3]	1.0 10^9	1.0 10^9	1.0 10^9
$\bar{t}_n^t$ [N/mm^2]	50.0	300.0	50.0
$\bar{t}_n^c$ [N/mm^2]	200.0	400.0	200.0
$\bar{t}_s, \bar{t}_t$ [N/mm^2]	90.0	200.0	65.0
G_c [N/m]	200.0	450.0	200.0

In Figures 23 and 24 the in-plane shear stresses in the die-support paddle and the lead frame are presented in the seventh cycle at a temperature of -20 °C. Due to the high strength of the glue between the chip and the die-support paddle high shear stresses are possible near the edge and the corner of the chip. The curvature of the die-paddle is the result of the difference in thermal expansion coefficients of the chip and the metal. Figures 25 to 27 present the delaminated areas at the three interface layers also in the seventh cycle. In the interface at r_3 = 1.45 mm delamination occurs at the edge of the die-support paddle (Figure 25) in the metal/epoxy interface, the location where the shear stress σ_{13} has its maximum value. From Figure 26 it is observed that the in-plane shear stresses that are shown in Figures 23 and 24 induce delamination fracture between die paddle and epoxy near the chip edge (r_2 = 5.0 mm) and the lead frame and the epoxy coating ($r_1 = r_2$ = 6.0 mm). Figures 28 to 31 show the delaminated area at -65.0 °C in cycles 1, 6, 7 and 8. They clearly indicate that the delamination between the chip and the epoxy at the top surface of the chip starts at the chip corner and progresses along the edges and towards the centre of the chip. This is in agreement with experimental observations.

Figure 32 shows SCAT-picture (SCAT is SCanning Acoustic Tomography) of the top surface of the chip after 500 temperature cycles. The delaminations areas at the corners of the chip are clearly visible.

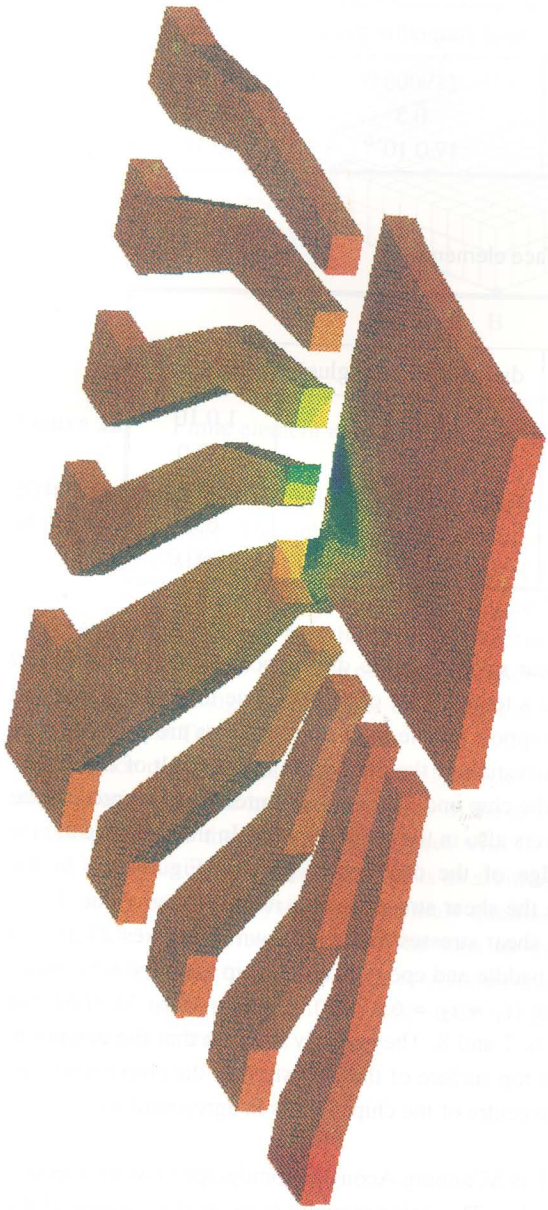

Figure 23 In-plane shear stresses σ_{12}

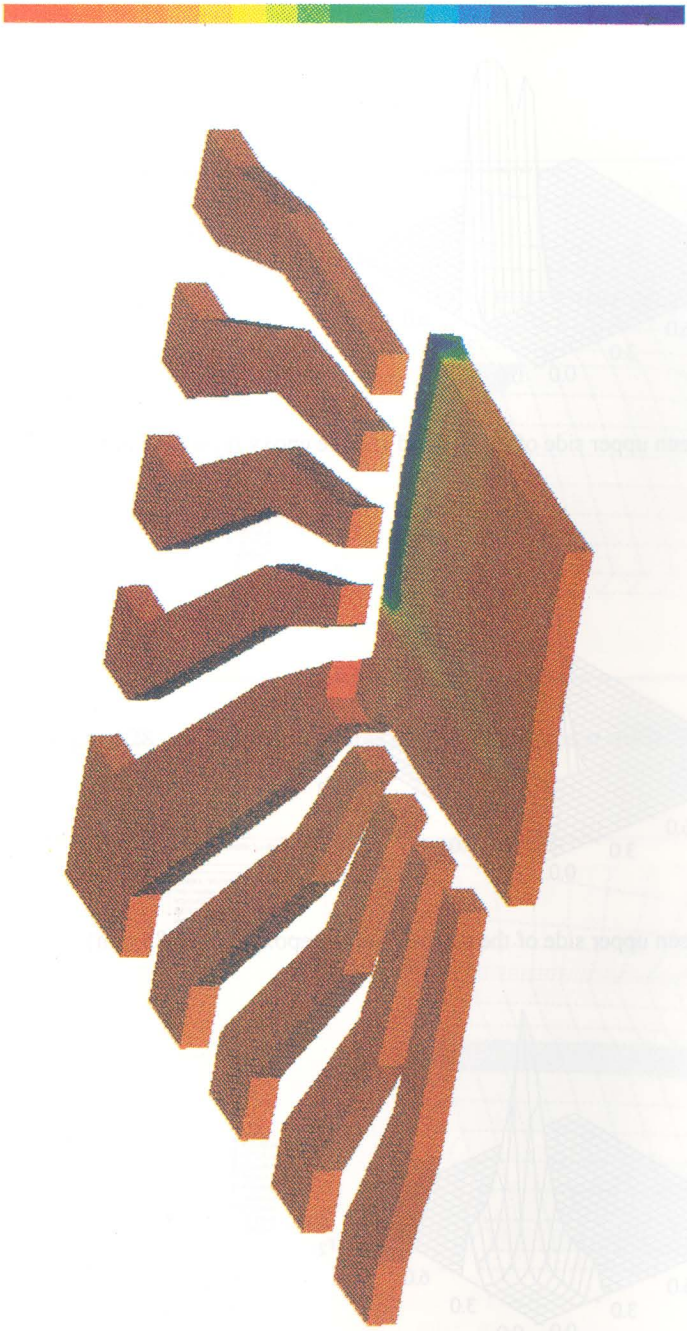

Figure 24 In-plane shear stresses σ_{13}

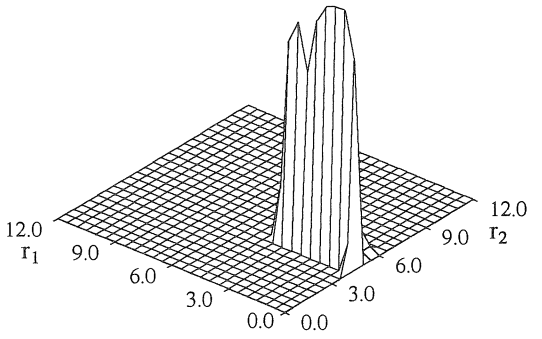

Figure 25 Delamination between upper side of the die-pad and the epoxy (r_3 = 1.45 mm).

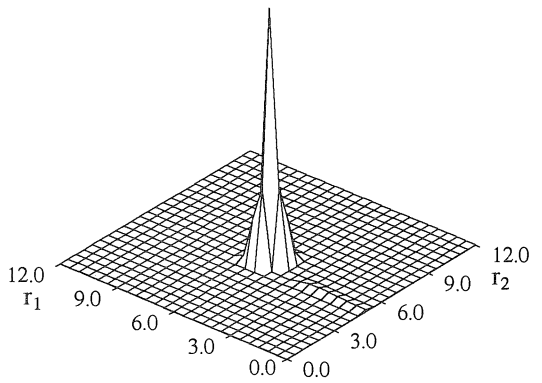

Figure 26 Delamination between upper side of the die-pad and the epoxy (r_3 = 1.85 mm).

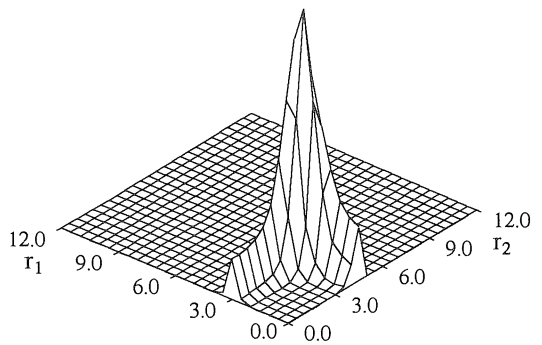

Figure 27 Delamination between upper side of the chip and the epoxy (r_3 = 2.25 mm).

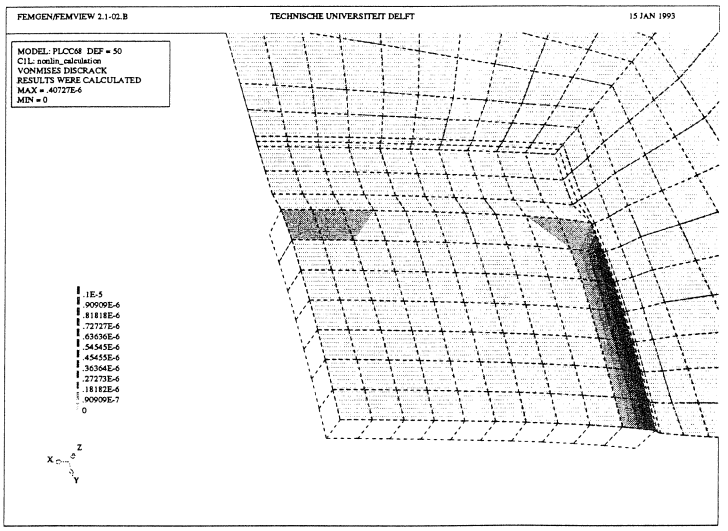

Figure 28 Delaminated area at the chip surface at -65.0 °C in the 1st cycle

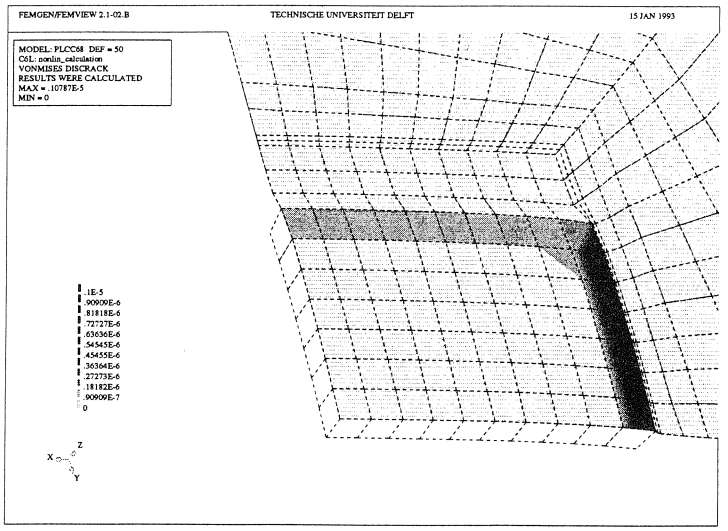

Figure 29 Delaminated area at the chip surface at -65.0 °C in the 6th cycle

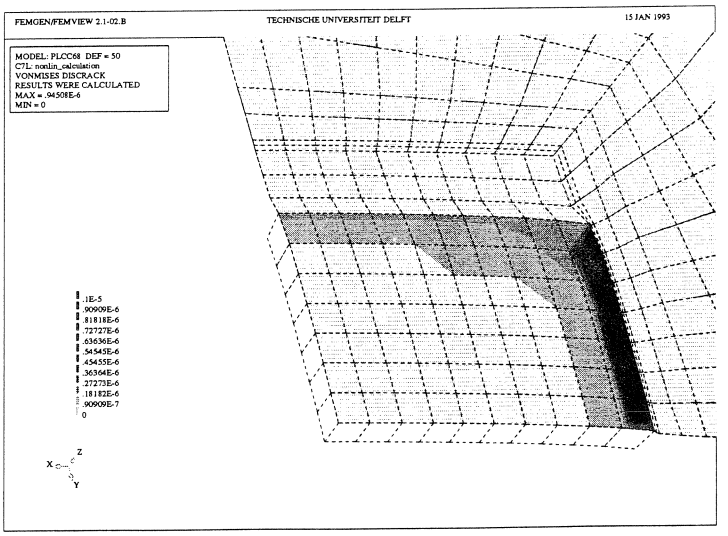

Figure 30 Delaminated area at the chip surface at -65.0 °C in the 7th cycle

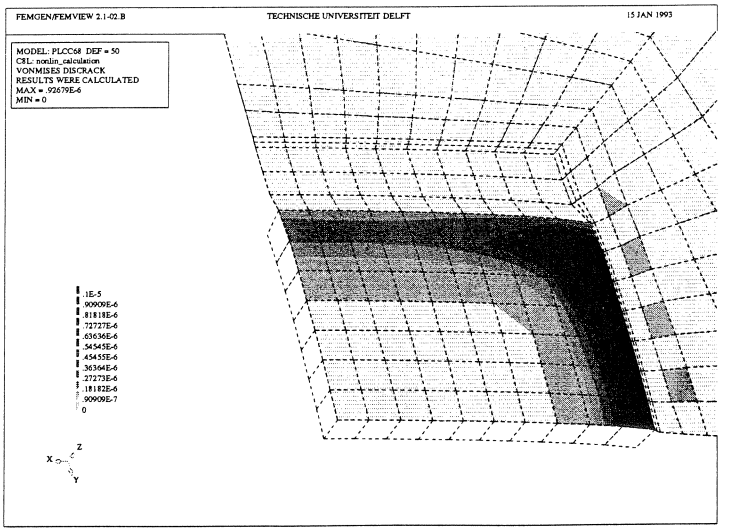

Figure 31 Delaminated area at the chip surface at -65.0 °C in the 8th cycle

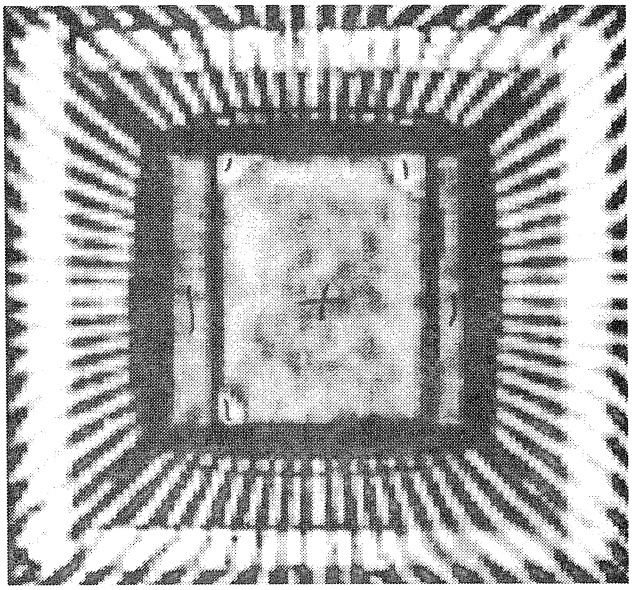

Figure 32 SCAT picture of the top chip surface after 500 temperature cycles

Acknowledgements

The authors would like to express their gratitude to Stefan Weihe of the Institute of Statics and Dynamics of Aerospace Structures of the University of Stuttgart and Richard van Gestel of the Electrical Engineering Department of the Delft University of Technology for the preparation of the finite element meshes shown in sections 4.2 and 4.3.

References

BAZANT, Z.P. and OH, B. (1983) - Crack band theory for fracture of concrete, *RILEM Mat. Struct.* **16**, pp. 155-177.

BEER, G. (1985) - An isoparametric joint/interface element for finite element analysis, *Int. J. Num. Meth. Engng.*, **21**, pp. 585-600.

BENALLAL, A., BILLARDON, R. and GEYMONAT, G. (1991) - 'Localization phenomena at the boundaries and interfaces of solids', *Proc. Third Int. Conf. Constitutive Laws for Engineering Materials: Theory and Applications*, Ed. C.S. Desai, Tucson, Arizona, pp. 387-390.

BORST, R. DE and ROTS, J.G. (1989) - Occurrence of spurious mechanisms in computations of strain-softening solids, *Engng. Comput.*, **6(4)**, pp. 272-280.

BORST, R. DE (1991) - Simulation of strain localisation: A reappraisal of the Cosserat continuum, *Engng. Comput.*, **8**, pp. 317-332.

BORST, R. DE and MUHLHAUS, H.-B. (1992) - Gradient-dependent plasticity: Formulation and algorithmic aspects, *Int. J. Num. Meth. Engng.*, **35**, pp. 521-539.

GENS, A., CAROL, I. and ALONSO, E.E. (1988) - An interface element formulation for the analysis of soil-reinforcement interaction, *Comput. Geotechnics*, **7**, pp. 133-151.

GENS, A., CAROL, I., and ALONSO, E.E. (1989) - 'Elasto-plastic model for joints and interfaces', *Proc. 2nd Int. Conf. Computational Plasticity, Vol. 2*, Eds. Owen D.R.J., Hinton, E. and Oñate, E., Pineridge Press, Swansea, pp. 1251-1264.

GESTEL, H.C.J.M., (1990) - Reliability research on IC packaging, *Tijdschrift van het Nederlands Electronica en Radiogenootschap*, **55(2)**, pp. 61-66.

GOODMAN, R.E., TAYLOR, R.L. and BREKKE, T.L. (1968) - A model for the mechanics of jointed rock, *ASCE J. Soil Mech. Found. Div.*, **94**, pp. 637-659.

HOHBERG, J.M. and BACHMANN, H. (1989) - 'A macro joint element for nonlinear arch dam analysis', *Numerical Methods in Geomechanics*, Ed. Swoboda, G., Balkema, Rotterdam, pp. 829-834.

HOHBERG, J.M. (1990) - A note on the spurious kinematic oscillations in FEM joint elements, *Earthq. Engng. Struct. Dynamics.*, **19**, pp. 773-779.

JONES, R.H., BOYD, J.G. and ALLEN, D.H. (1991) - *Micromechanical analysis of inelastic composites including the effects of matrix viscoplasticity and evolving damage*, Report CMC No. 91-14, Texas A&M University, Center for Mechanics of Composites.

KEUSER, M., MEHLHORN, G. and CORNELIUS, V (1983) - Bond between prestressed steel and concrete: Computer analysis using ADINA, *Comp. Struct.*, **17**, pp. 669-676.

MEHLHORN, G., KOLLEGGER, J., KEUSER, M. and KOLMAR, W. (1985) - Nonlinear contact problems - A finite element approach implemented in ADINA, *Comp. Struct.*, **21**, pp. 69-80.

MUHLHAUS, H.-B. and VARDOULAKIS, I. (1987) - The thickness of shear bands in granular materials, *Géotechnique*. **37** , 271-283.

MUHLHAUS, H.-B. and AIFANTIS, E.C. (1991) - A variational principle for gradient plasticity, *Int. J. Solids Structures*, **28**, pp. 845-858.

NGO, D., and SCORDELIS, A.C. (1967) - Finite element analysis of reinforced concrete beams, *J. Amer. Concrete Institute*, **64**, pp. 152-163.

PIJAUDIER-CABOT, G. and BAZANT, Z.P. (1987) - Nonlocal damage theory, *ASCE J. Eng. Mech.*, **113**, pp. 1512-1533.

QIU, X., PLESHA, M.E. and MEYER, D.W. (1992) - Stiffness matrix integration rules for contact-friction finite elements, *Comp. Meth. Appl. Mech. Engng.*, to appear.

ROELFSTRA, P.E. (1989) - 'Simulation of strain localization processes with numerical concrete', *Cracking and Damage. Strain Localization and Size Effect*, Eds. Mazars, J. and Bažant, Z.P., Elsevier Science Publishers, London, pp. 79-90.

RODIC, T. and OWEN, D.R.J. (1989) - 'A plasticity theory of friction and joint elements', *Proc. 2nd Int. Conf. Computational Plasticity, Vol. 2*, Eds. Owen D.R.J., Hinton, E. and Oñate, E., Pineridge Press, Swansea, pp. 1043-1062.

ROTS, J.G. (1988) - *Computational modelling of concrete fracture,* Dissertation, Delft University of Technology, Delft.

SCHAEFER, H. (1975) - A contribution to the solution of contact problems with the aid of bond elements, *Comp. Meth. Appl. Mech. Engng.*, **6**, pp. 335-354.

SCHELLEKENS, J.C.J. (1990) - *Interface elements in finite element analysis,* Report 25.2-90-2-17, Delft University of Technology, Delft.

SCHELLEKENS, J.C.J. and BORST, R. DE (1993) - On the integration of interface elements, *Int. J. Num. Meth. Engng.*, **36**, pp. 43-66.

SCHELLEKENS, J.C.J. (1992) - *Computational strategies for composite structures,* Dissertation, Delft University of Technology, Delft.

SLUYS, L.J. (1992) - *Wave propagation, localisation and dispersion in strain softening solids,* Dissertation, Delft University of Technology, Delft.

WEIHE, S. (1992) - *Numerical simulation of composite failure. Part I: Random generation of 2-D fiber composites,* ISD-Report 92-W-01, ISD, University of Stuttgart, Stuttgart.

WILLAM, K.J. (1984) - 'Experimental and computational aspects of concrete failure', *Proc. Int. Conf. Computer Aided Analysis and Design of Concrete Structures,* Eds. Damjanić F. *et al.*, Pineridge Press, Swansea, pp. 33-70.

WILLAM, K.J. (1989) - 'Simulation issues of distributed and localized failure computations', *Cracking and Damage. Strain Localization and Size Effect,* Eds. Mazars, J. and Bažant, Z.P., Elsevier Science Publishers, London, pp. 363-378.